AIAA JOURNAL
Vol. 42, No. 2, February 2004

Photonic Control of Cylindrical Shells with Electro-Optic Photostrictive Actuators

Hui-Ru Shih* and Roderick Smith†
Jackson State University, Jackson, Mississippi 39217
and
Horn-Sen Tzou‡
University of Kentucky, Lexington, Kentucky 40506

Photostrictive actuator, which can directly turn light energy into mechanical energy, is a new promising photoactuation technique for active vibration control of flexible structures. It offers the advantage of generating distributed actuation strain without connecting any electric lead wires. Photonic control of flexible cylindrical shells using discrete photostrictive actuators is investigated, and the photoactuation effectiveness is evaluated. A coupled optopiezothermoelastic shell theory is presented that incorporates photovoltaic, pyroelectric, piezoelectric, and thermal effects and has the capability to accurately predict the response of a shell to a command illumination applied to the photostrictive actuators. Expressions for the photogenerated forces and moments have been developed. Governing equations are formulated. Solution procedures based on the modal analysis technique are outlined. The detailed actuator control effectiveness is evaluated with respect to actuator placements. It is shown that by properly positioned the actuators the system performance can be improved. Numerical simulation results also show that the membrane control action is more significant than the bending control action. The circumferential membrane control action dominates, and the photonic control effectiveness is only slightly reduced by the removal of all of the actuator patches along the longitudinal direction.

I. Introduction

In recent years, significant effort has been directed toward integrating smart materials (such as piezoelectrics, shape-memory alloys, electrorheological fluids, etc.) with structures in such a way that the structures transform from completely passive systems to active adaptive systems. Smart structures have shown promise and practicality for active shape and vibration control of high performance structures. Crawley,[1] Rogers,[2] and Tzou[3] provide detailed overviews of the state of smart structure technologies. However, these smart material sensor/actuator systems are hard wired. In many operating environments, the metallic signal wires are likely to attract electric noises that will contaminate the control signals. To remedy this situation, optically driven actuators have been proposed.[4–7] The optical actuator system has neither electric lead wires nor electric circuits, so that it is relatively immune from electric/magnetic disturbances. Thus, the optical actuator is ideal for being used in harsh environmental conditions with strong magnetic and electric disturbances. The development of accurate and reliable mathematical model of photostrictive actuators to simulate the optopiezothermoelastic behavior is of most importance.

Photostrictive materials, like PLZT, are capable of producing strains under irradiation of high-energy lights. This functionality, which would bypass the need for an electrical energy source, eliminates connection wires and can replace a conventional hard-wired electromechanical actuator with the optically triggered, contactless actuator. PLZT is a special ceramic compound made from lead (Pb), lanthanum (La), zirconium (Zr) and titanium (Ti). The photostrictive actuator exhibits many advantages (including immunity to electromagnetic interference, noncontact actuation, lightweight and small size) over the widely used electromechanical actuators. The PLZT-actuated beams, curved beams, and plate structures have been investigated recently.[5–10]

This study provides insights to the optical actuation effect of photostrictive materials applied to photonic control of shell structures. In this paper, a simply supported cylindrical shell consisting of photostrictive optical actuators is considered. Analytical formulations of the governing equations are derived, which account for the coupled mechanical, electrical, thermal, and optical responses of photostrictive smart shell structures. Solution procedures based on the modal analysis techniques are presented. As will be shown in this paper, the placement of actuators is one of the main issues in the design of adaptive structures. The effectiveness of a smart structure decisively depends on the amount and distribution of active materials on the host structure. In this study, five actuator configurations are evaluated, and the results are compared. The comparison shows that the increased control effectiveness can be achieved by placing the actuators at better-selected locations. The study also suggests the circumferential β actuator (actuator along the β direction) is much more effective than the longitudinal x actuator for vibration control of cylindrical shells.

II. Governing Material Equations

The response of photostrictive materials involves coupled mechanical, optical, and electrical behavior. Structures with surface bonded photostrictive optical actuators exhibit very complex coupled physical behavior. To ensure the integrity and reliability of these structures, it is essential to develop tools that can accurately model the strains experienced by the actuators, as well as the host structures. In this section, a mathematical model for predicting behavior of optical actuators is presented.

An optical actuator is made up of a photostrictive wafer as shown in Fig. 1. The polarization is in the $\hat{z}$ direction, and the $\hat{x}$–$\hat{y}$ planes are the planes of the electrodes. The high-energy illumination irradiated on the distributed optical actuator induces a photodeformation process. The photodeformation process involves two fundamental effects: the photovoltaic effect (light into electricity) and the converse piezoelectric effect (electricity into motion). The light irradiated on the optical actuator first induces a current, opposite to the polarized direction. This current generates a voltage between the two surface

Received 19 March 2003; revision received 21 August 2003; accepted for publication 3 September 2003.

*Professor, Department of Technology; huiru.shih@jsums.edu. Member AIAA.
†Research Assistant, Department of Technology.
‡Professor, Department of Mechanical Engineering.

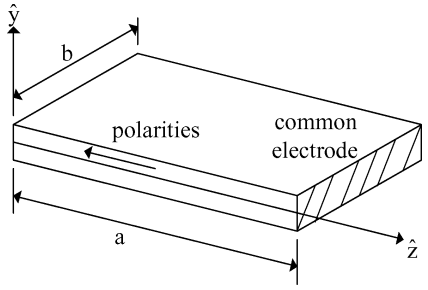

Fig. 1 Photostrictive optical actuator.

electrodes. This phenomenon is known as the photovoltaic effect. The induced photovoltaic voltage induces actuation strains as the result of the converse piezoelectric effect. The induced photovoltaic electric field $E_l(t)$ at instant t can be written as

$$E_l(t) = (E_s - E_0)\left[1 - e^{\frac{-\alpha I_0 t}{a_s}}\right] \tag{1}$$

where E_s is the saturated photovoltaic field, E_0 denotes an initial electric field between the electrodes of the optical actuator, $a_s = a/b$ (length/width) is the aspect ratio, I_0 is the constant illumination intensity, and α is optical actuator constant. During the light-induced charge appearing on the surface electrodes, voltage leakage is likely to occur. The voltage leakage can be estimated by

$$E_{\text{leakage}} = E_l e^{-\varphi t} \tag{2}$$

where φ is a constant related to voltage leakage. The existing voltage between the two surface electrodes can be determined by the induced photovoltaic voltage along with the voltage leakage. If the light intensity $I(t)$ is a function of time and $E_l(t_j)$ denotes the induced electric field at time t_j while $I(t)$ remains constant during the interval Δt, then the electric field $E_l(t_j)$, which corresponds to $t_j = t_{j-1} + \Delta t$, can be approximated by

$$E_l(t_j) = E_l(t_{j-1}) + [E_s - E_l(t_{j-1})]\frac{\alpha}{a_s} I(t_j) e^{-\frac{\alpha}{a_s} I(t_j)\Delta t} \cdot \Delta t - E_l(t_{j-1})\varphi e^{-\varphi \Delta t} \cdot \Delta t \tag{3}$$

When the light illumination is irradiating on the surface of an optical actuator, the high-energy light not only induces an electric field but also heats up the actuator. The actuator temperature can be defined in a difference equation:

$$\theta(t_j) = \theta(t_{j-1}) + \Delta\theta = \theta(t_{j-1}) + \frac{[I(t_j)P - \gamma\theta(t_{j-1})]\Delta t}{H + \gamma \Delta t} \tag{4}$$

where $\theta(t_j)$ is the actuator body temperature at t_j, $\Delta\theta$ is the temperature variation, P is the absorbed heat from the light illumination, H is the heat capacity of the actuator, and γ is the heat transfer rate from the actuator to the host structure.

The temperature rise can trigger the pyroelectric effect from which an additional voltage is generated. $E_\theta(t)$, the electric field associated with pyroelectric effect's contribution, can be determined from

$$E_\theta(t) = (P_n/\varepsilon)\theta(t) \tag{5}$$

where P_n is the pyroelectric constant and ε is the permittivity. Although the heat can trigger the pyroelectric effect and further enhance the strain generation, the heat also interferes with photodeformation process. The photo effect decreases, as the actuator temperature becomes higher.

Photostrictive optical actuators, when unconstrained and activated by applying a high-intensity light, develop extensional strain along their polarization direction. By considering all of the effects, the overall magnitude of the induced strains developed in the actuator in response to an applied light is then obtained as

$$\bar{s}(t) = d_{33}[E_l(t) + E_\theta(t)] - \lambda\theta(t)/Y_a \tag{6}$$

Table 1 Material properties of the photostrictive actuators

Property	Value
Saturated electric field	$E_s = 2.43 \times 10^5$ V/m
Mass density	$\rho_a = 7.6 \times 10^3$ kg/m^3
Young's modulus	$Y_a = 6.3 \times 10^{10}$ N/m^2
Optical actuator constant	$\alpha = 0.02772$ cm^2/(w s)
Voltage leakage constant	$\beta = 0.01$ V/s
Power of absorbed heat	$P = 0.23 \times 10^3$ cm^2/s
Piezoelectric strain constant	$d_{33} = 1.79 \times 10^{-10}$ m/V
Heat capacity	$H = 16$ w/°C
Heat-transfer rate	$\gamma = 0.915$w/°C s
Stress-temperature constant	$\lambda = 6.8086 \times 10^4$ N/m^2°C
Pyroelectric constant	$P_n = 0.25 \times 10^{-4}$ C/m^2°C
Electric permittivity	$\varepsilon = 1.65 \times 10^{-8}$ F/m

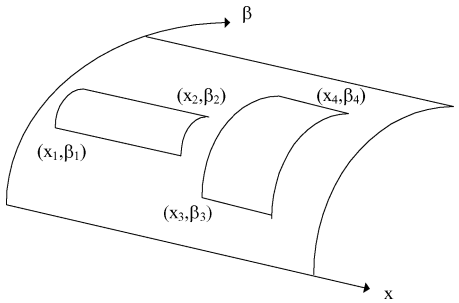

Fig. 2 Shell with photostrictive actuators.

where d_{33} is a piezoelectric constant, λ is a thermal stress coefficient, and Y_a is the Young's modulus of the opto-electromechanical actuator. The mathematical model of photostrictive actuators is used for system analysis. The parameters used for the investigation reported in this paper are shown in Table 1. Note that these material parameters are calibrated and validated with experimental data before used in simulation studies.[9] Fundamental design configurations of distributed photostrictive actuators are also similar to those of earlier studies.[9,10]

III. Modeling of Cylindrical Shell Actuators

Based on the photodeformation process discussed earlier, this section focuses on modeling of a simply supported cylindrical shell with two pairs of surface-bonded optical actuators (Fig. 2). A cylindrical coordinate system (x, β, z) is employed, where x, β, and z denote the longitudinal, circumferential, and transverse directions, respectively. The variables u_1, u_2, and u_3 are the displacements along the x, β, and z axes, respectively. In this study, it is assumed that the actuator patches are bonded perfectly to the cylindrical shell, and the thickness of the actuator patches h_a is much less than the thickness of the shell. An actuator patch with edges defined by x_1, x_2, β_1, and β_2, as shown in Fig. 2, produces a strain over its area. If the polarity of the actuator is in the x direction, the actuator can be activated to produce a strain in the x direction. As a result, the actuator can generate a membrane force. The photodeformation generated force is the product of direct stress $Y_a\bar{s}$, and the thickness of the actuator patch:

$$N^c_{xx} = \begin{matrix} h_a Y_a \bar{s}, \\ 0, \end{matrix} \quad \begin{matrix} x_1 \le x \le x_2 \quad \beta_1 \le \beta \le \beta_2 \\ \text{elsewhere} \end{matrix} \tag{7}$$

or, expressing Eq. (7) in one equation by using a step function $H(\cdot)$,

$$N^c_{xx} = h_a Y_a \bar{s}[H(x-x_1) - H(x-x_2)]\cdot[H(\beta-\beta_1) - H(\beta-\beta_2)] \tag{8}$$

The bending moment induced by the actuator can be expressed as the product of the membrane force and the distance between the middle surface of the actuator patch and the middle surface of the

shell, that is,

$$M^c_{xx} = [(h + h_a)/2]h_a Y_a \bar{s} \times [H(x - x_1) - H(x - x_2)] \cdot [H(\beta - \beta_1) - H(\beta - \beta_2)] \quad (9)$$

where h is the shell thickness.

In a similar fashion, for another actuator patch with edges x_3, x_4, β_3, β_4 and polarity in the β direction (see Fig. 2), the photo-induced membrane force $N^c_{\beta\beta}$ and bending moment $M^c_{\beta\beta}$ in the shell are

$$N^c_{\beta\beta} = h_a Y_a \bar{s}[H(x - x_3) - H(x - x_4)] \cdot [H(\beta - \beta_3) - H(\beta - \beta_4)] \quad (10)$$

$$M^c_{\beta\beta} = [(h + h_a)/2]h_a Y_a \bar{s} \times [H(x - x_3) - H(x - x_4)] \cdot [H(\beta - \beta_3) - H(\beta - \beta_4)] \quad (11)$$

With the definitions of forces and moments, it is now possible to write the equations of motion for the cylindrical shell laminated with photostrictive actuators. It is assumed that the added mass and stiffness of the actuators are neglected. Using the corresponding Lamé parameters and the radii of curvature,[11,12] the three governing equilibrium equations are

$$-\frac{\partial N_{xx}}{\partial x} - \frac{1}{R}\frac{\partial N_{x\beta}}{\partial \beta} + \rho h \frac{\partial^2 u_1}{\partial t^2} = \frac{\partial N^c_{xx}}{\partial x} \quad (12)$$

$$-\frac{\partial N_{x\beta}}{\partial x} - \frac{1}{R}\frac{\partial N_{\beta\beta}}{\partial \beta} - \frac{1}{R}\left(\frac{\partial M_{x\beta}}{\partial x} + \frac{1}{R}\frac{\partial M_{\beta\beta}}{\partial \beta}\right) + \rho h \frac{\partial^2 u_2}{\partial t^2} = \frac{1}{R}\frac{\partial N^c_{\beta\beta}}{\partial \beta} + \frac{1}{R^2}\frac{\partial M^c_{\beta\beta}}{\partial \beta} \quad (13)$$

$$-\frac{\partial^2 M_{xx}}{\partial x^2} - \frac{2}{R}\frac{\partial^2 M_{x\beta}}{\partial x \partial \beta} - \frac{1}{R^2}\frac{\partial^2 M_{\beta\beta}}{\partial \beta^2} + \frac{N_{\beta\beta}}{R} + \rho h \frac{\partial^2 u_3}{\partial t^2} = \frac{\partial^2 M^c_{xx}}{\partial x^2} - \frac{N^c_{\beta\beta}}{R} + \frac{1}{R^2}\frac{\partial^2 M^c_{\beta\beta}}{\partial \beta^2} \quad (14)$$

where N_{ij} and M_{ij} denote the elastic forces and moments, respectively; R is the radius of the shell; and ρ is the shell mass density. The elastic force and moment resultants of circular cylindrical shells are defined as

$$N_{xx} = \frac{Eh}{1 - \nu^2}\left[\frac{\partial u_1}{\partial x} + \frac{\nu}{R}\left(\frac{\partial u_2}{\partial \beta} - u_3\right)\right] \quad (15)$$

$$N_{\beta\beta} = \frac{Eh}{1 - \nu^2}\left[\frac{1}{R}\left(\frac{\partial u_2}{\partial \theta} - u_3\right) + u_2 \frac{\partial u_1}{\partial x}\right] \quad (16)$$

$$N_{x\beta} = \frac{Eh}{2(1 + \nu)}\left(\frac{\partial u_2}{\partial x} + \frac{1}{R}\frac{\partial u_1}{\partial \beta}\right) \quad (17)$$

$$M_{xx} = D\left[\frac{\partial^2 u_3}{\partial x^2} + \frac{\nu}{R^2}\left(\frac{\partial u_2}{\partial \beta} + \frac{\partial^2 u_3}{\partial \beta^2}\right)\right] \quad (18)$$

$$M_{\beta\beta} = D\left[\frac{1}{R^2}\left(\frac{\partial u_2}{\partial \beta} + \frac{\partial^2 u_3}{\partial \beta^2}\right) + \nu \frac{\partial^2 u_3}{\partial x^2}\right] \quad (19)$$

$$M_{x\beta} = D(1 - \nu)\left(\frac{\partial u_2}{\partial x} + \frac{\partial^2 u_3}{\partial x \partial \beta}\right)\frac{1}{R} \quad (20)$$

where ν and D are the Poisson's ratio and the flexural shell stiffness, respectively.

IV. Distributed Control Actions

Assume that the total response $u_i(x, \beta, t)$ of the shell is composed of all participating modes of the shell:

$$u_i(x, \beta, t) = \sum_{m=1}^{\infty}\sum_{n=1}^{\infty} \eta_{imn}(t) U_{imn}(x, \beta), \qquad i = x, \beta, z \quad (21)$$

where η_{mn} is the modal participation factor, m is the half-wave number in the x direction, n is the half-wave number in the β direction, and U_{mn} is the modal function. Because the transverse oscillation is the primary oscillation of interest, only the transverse oscillation is considered in this study. For a simply supported cylindrical shell, the transverse modal function is defined by

$$U_{mn} = \sin(m\pi x/L)\sin(n\pi\beta/\beta^*) \quad (22)$$

where L is cylindrical shell length and β^* is shell curvature angle. Substituting the modal expansion equation into Eq. (14), integrating over the whole shell surface, and applying the modal orthogonality, the mnth modal equation of cylindrical shell can be found as

$$\ddot{\eta}_{mn} + 2\xi_{mn}\omega_{mn}\dot{\eta}_{mn} + \omega^2_{mn}\eta_{mn} = F_{mn} \quad (23)$$

where ξ_{mn} is the damping ratio and ω_{mn} is the natural frequency of the mnth mode. The parameter F_{mn} is called the distributed modal force and is defined as

$$F_{mn} = \frac{4}{\rho h L R \beta^*}\int_0^L \int_0^{\beta^*} \times \left(\frac{\partial^2 M^c_{xx}}{\partial x^2} - \frac{N^c_{\beta\beta}}{R} + \frac{1}{R^2}\frac{\partial^2 M^c_{\beta\beta}}{\partial \beta^2}\right) U_{mn}(x, \beta) R \, dx \, d\beta \quad (24)$$

Substituting Eqs. (9–11), respectively, into the first, second, and third integral terms of the preceding equation, each term can be rewritten as

$$\frac{4}{\rho h L R \beta^*}\int_0^L \int_0^{\beta^*} \frac{\partial^2 M^c_{xx}}{\partial x^2} U_{mn}(x, \beta) R \, dx \, d\beta = \frac{2(h + h_a)h_a}{\rho h L R \beta^*} Y_a \bar{s} \int_0^L \int_0^{\beta^*} \frac{\partial^2}{\partial x^2}\{[H(x - x_1) - H(x - x_2)] \cdot [H(\beta - \beta_1) - H(\beta - \beta_2)]\} U_{mn}(x, \beta) R \, dx \, d\beta = \frac{-2(h + h_a)h_a Y_a}{\rho h L \beta^*}\bar{s}\frac{m\beta^*}{nL}\left[\left(\cos\frac{m\pi x_1}{L} - \cos\frac{m\pi x_2}{L}\right) \times \left(\cos\frac{n\pi\beta_1}{\beta^*} - \cos\frac{n\pi\beta_2}{\beta^*}\right)\right] = -\tilde{M}_{mnx}\bar{s} \quad (25)$$

$$\frac{4}{\rho h L R \beta^*}\int_0^L \int_0^{\beta^*} \frac{N^c_{\beta\beta}}{R} U_{mn}(x, \beta) R \, dx \, d\beta = \frac{4h_a}{\rho h L R^2 \beta^*} Y_a \bar{s} \int_0^L \int_0^{\beta^*} \{[H(x - x_3) - H(x - x_4)] \cdot [H(\beta - \beta_3) - H(\beta - \beta_4)]\} U_{mn}(x, \beta) R \, dx \, d\beta = \frac{4h_a Y_a}{\rho h L R \beta^*}\bar{s}\frac{\beta^* L}{mn\pi^2}\left[\left(\cos\frac{m\pi x_3}{L} - \cos\frac{m\pi x_4}{L}\right) \times \left(\cos\frac{n\pi\beta_3}{\beta^*} - \cos\frac{n\pi\beta_4}{\beta^*}\right)\right] = \tilde{N}_{mn\beta}\bar{s} \quad (26)$$

$$\frac{4}{\rho h L R \beta^*}\int_0^L\int_0^{\beta^*}\frac{1}{R^2}\frac{\partial^2 M^c_{\beta\beta}}{\partial\beta^2}U_{mn}(x,\beta)R\,\mathrm{d}x\,\mathrm{d}\beta$$

$$=\frac{2(h+h_a)h_a}{\rho h L R^3\beta^*}Y_a\bar{s}\int_0^L\int_0^{\beta^*}\frac{\partial^2}{\partial\beta^2}\{[H(x-x_3)$$

$$-H(x-x_4)]\cdot[H(\beta-\beta_3)-H(\beta-\beta_4)]\}U_{mn}(x,\beta)R\,\mathrm{d}x\,\mathrm{d}\beta$$

$$=\frac{-2(h+h_a)h_aY_a}{\rho h L R^2\beta^*}\bar{s}\frac{nL}{m\beta^*}\left[\left(\cos\frac{m\pi x_3}{L}-\cos\frac{m\pi x_4}{L}\right)\right.$$

$$\left.\left(\cos\frac{n\pi\beta_3}{\beta^*}-\cos\frac{n\pi\beta_4}{\beta^*}\right)\right]=-\tilde{M}_{mn\beta}\bar{s} \tag{27}$$

In the preceding three equations, the symbols $\tilde{M}_{mnx}$, $\tilde{N}_{mn\beta}$, and $\tilde{M}_{mn\beta}$ are used to simplify the expressions. Employing those symbols, the distributed modal force F_{mn} becomes

$$F_{mn}=-\bar{s}(\tilde{M}_{mnx}+\tilde{M}_{mn\beta}+\tilde{N}_{mn\beta}) \tag{28}$$

As shown by Eqs. (25–28), the distributed modal force F_{mn} depends on the mode numbers, the spatial distribution, the actuator material properties, and the locations and dimensions of the actuator patches. In view of Eq. (28), also note that the first two terms are related to the bending effect, and the third term is contributed by the membrane effect. By introducing a control factor, which indicates the modal bending and membrane control effectiveness of the actuators, defined by

$$\tilde{F}_{mn}=\tilde{M}_{mnx}+\tilde{M}_{mn\beta}+\tilde{N}_{mn\beta} \tag{29}$$

the modified *mn*th modal equation can be expressed as

$$\ddot{\eta}_{mn}+2\xi_{mn}\omega_{mn}\dot{\eta}_{mn}+\omega^2_{mn}\eta_{mn}=-\bar{s}\tilde{F}_{mn} \tag{30}$$

Equation (30) can be used to determine the response of the cylindrical shell to the control forces generated by photostrictive actuators.

V. Photonic Control of Cylindrical Shells

In this study, a constant light intensity control is used. The light intensity $I(t)$ is defined as

$$I(t)=G[\max|\dot{\eta}_{mn}(t)|] \tag{31}$$

where G is the feedback gain. The induced forces and moments caused by the applied light are used to counteract the shell oscillation. The direction of the light should be carefully controlled. For a photostricitve smart shell, the paired actuators are respectively placed on the top and bottom surfaces of the shell. By shining a light on one surface, the bonded actuators can induce a positive control action. However, when the light irradiates on the other surface the control action will be negative. As a result, both positive and negative control actions can be generated by flashing alternating pulse of light on either side of the shell. Hence, Eq. (30) can be rewritten in the form

$$\ddot{\eta}_{mn}+2\xi_{mn}\omega_{mn}\dot{\eta}_{mn}+\omega^2_{mn}\eta_{mn}=-\bar{s}\tilde{F}_{mn},\qquad\dot{\eta}_{mn}>0 \tag{32}$$

$$\ddot{\eta}_{mn}+2\xi_{mn}\omega_{mn}\dot{\eta}_{mn}+\omega^2_{mn}\eta_{mn}=\bar{s}\tilde{F}_{mn},\qquad\dot{\eta}_{mn}<0 \tag{33}$$

or, rewriting in a more convenient way,

$$\ddot{\eta}_{mn}+2\xi_{mn}\omega_{mn}\dot{\eta}_{mn}+\omega^2_{mn}\eta_{mn}+\mathrm{sgn}(\dot{\eta}_{mn})(\bar{s}\tilde{F}_{mn})=0 \tag{34}$$

where sgn is a signum function $\mathrm{sgn}(\cdot)=1$ when its argument is positive and $\mathrm{sgn}(\cdot)=-1$ when the argument is negative.

VI. Case Study

Based on the theoretical analysis presented in the preceding sections, a systematic study is conducted to evaluate the photonic control effectiveness on a simply supported shell with surface-bonded photostricitve actuators. The shell is made of aluminum and has the following geometric and material parameters: $L=1.2$ m, $R=1.0$ m, $\beta^*=\pi/3$, $h=0.5$ mm, $Y=69$ GPa, and $\rho=2710$ kg/m^3. The photostrictive wafers with thickness of 0.1 mm are bonded symmetrically over the top and bottom surfaces of the shell. The material properties of the actuator are presented in Table 1. All of the material constants of photostrictive actuators have been calibrated based on the laboratory experiments.[9]

In this study, it is assumed that the system has no inherent damping, and the photodeformation-induced active damping exclusively contributes to the vibration control. Because no structural damping is taken into account, the amplitudes of the uncontrolled shell do not decay. The response of the shell to photostrictive activation can be calculated from Eq. (34). Note that the in-plane displacements are not considered in this analysis because the transverse oscillation dominates the dynamic response.

A. Time History Analysis

In general, the placement of the actuators should be located in the regions of high structural surface strains. Placing the actuator at optimally selected locations enhances control effectiveness of cylindrical shells. However, the high-vibration and high-strain areas of the structural modes are seldom collected in one area, and thus a single actuator located there can seldom control all modes. In most structures, the high-vibration modes are located in different areas. A location collected with several modes might just be a node position of one specific mode. An actuator bonded there will therefore completely fail to control the latter mode. To prevent these problems, the use of an array of segmented actuators is proposed. Three different configurations of actuators were evaluated, and their layouts (top view) on cylindrical shells are illustrated in Figs. 3a–3c.

1. *Configuration 1*

For configuration 1, three actuators were symmetrically placed at the center of each shell surface. To study the effect of the actuator patches on the dynamic response of shell, a finite element model (using ANSYS) was developed. The first natural frequency of the elastic shell was calculated to be 59.98 Hz. When the presence of actuators was considered, the frequency of the shell increases to 60.75 Hz. This is because the system is stiffened by adding the photostrictive patches. However, the frequency change is less than 1.3%, which is practically insignificant. Therefore, the initially developed mathematical model (neglecting the effects of the patches) suffices for the present study.

To compare the control effectiveness, the control factor defined by Eq. (29) is calculated for modes (1, 1), (1, 2), (2, 1), and (2, 2). The results are given in Table 2. The control factor is used as an index for system's active control authority (the larger the better). The center of the shell is the location of the highest strain for the (1, 1) mode. When the actuators are placed at this location, the control effectiveness is greater. To observe the transient time history responses, an initial displacement of 1.0×10^{-3} m is imposed, and the snap-back responses are calculated. It is apparent from Fig. 4 that the (1, 1) mode is completely controlled. As far as the (2, 1) mode is concerned, the actuator is located symmetrically across the (2, 1) nodal line at $L/2$. The parallel actuator edges cancel each other when subjected to identical light irradiations. The value of control factor is equal to zero, as shown in Table 2. Thus, in this configuration the (2,1) mode is uncontrollable. An examination of the results presented in Table 2 reveals that the (1, 2) and (2, 2) modes also cannot be controlled. From the results of Fig. 4 and Table 2, it appears that the center-located actuators can control the symmetric modes ($m=1, 3, 5, \ldots$; $n=1, 3, 5, \ldots$), whereas the asymmetric modes ($m=2, 4, 6, \ldots$; $n=2, 4, 6, \ldots$,) are not controlled at all.

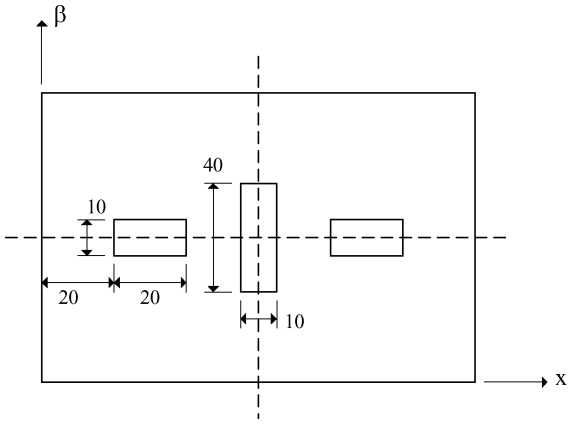

Fig. 3a Actuator configuration 1 (unit: centimeters) on the cylindrical shell (top view). Dimensions of the shell: $L = 1.2$ m, $R = 1.0$ m, and $\beta^* = \pi/3$.

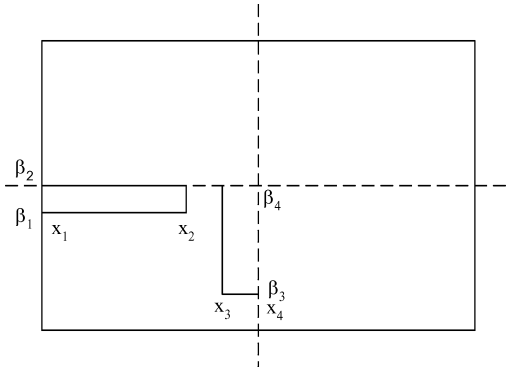

Fig. 3b Configuration 2.

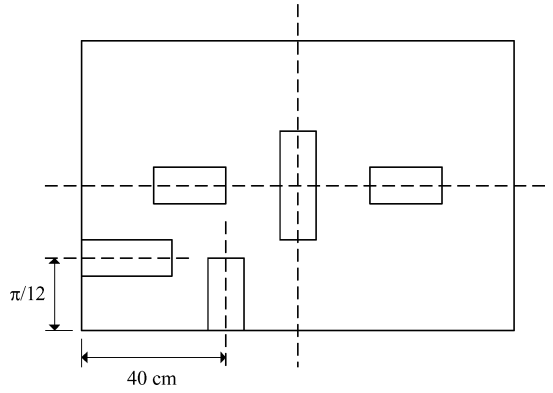

Fig. 3c Configuration 3.

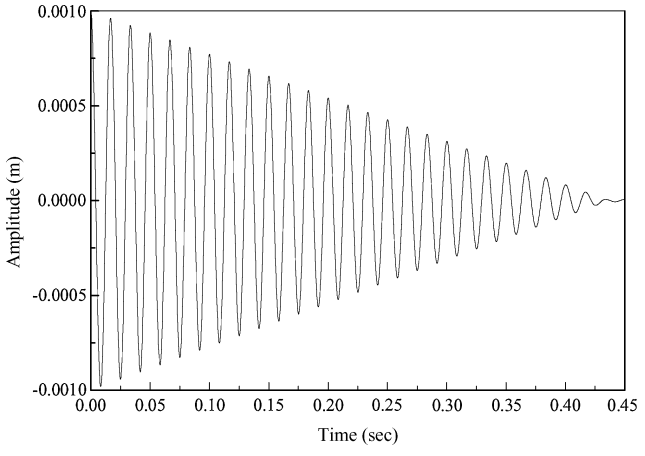

Fig. 4 Mode (1, 1) response, configuration 1.

Table 2 Control factors of configuration 1

Mode	Control factor
(1, 1)	2.018E5
(1, 2)	0.0
(2, 1)	0.0
(2, 2)	0.0

Table 3 Control factors of configuration 2

Mode	Control factor
(1, 1)	1.618E5
(1, 2)	1.550E5
(2, 1)	4.307E4
(2, 2)	4.048E4

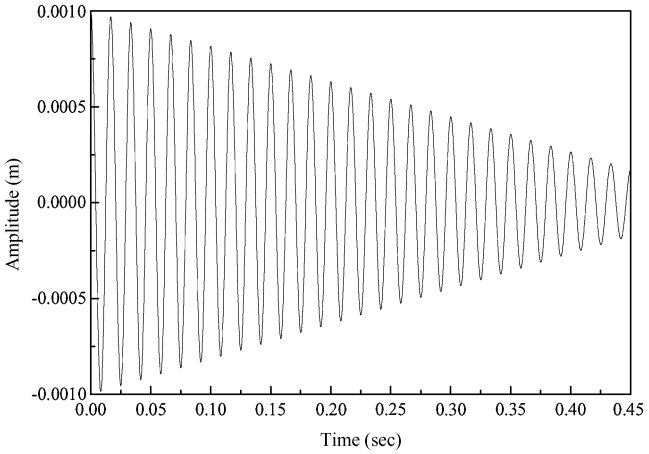

Fig. 5 Mode (1, 1) responses, configuration 2.

2. Configuration 2

It can be inferred from the preceding results that in order to ensure the controllability for most of the modes the actuators need to be placed unsymmetrically. For the second case of configuration 2, two actuators were placed at $x_1 = 0.0$ m, $x_2 = 0.4$ m, $\beta_1 = 2\pi/15$, $\beta_2 = \pi/6$, $x_3 = 0.5$ m, $x_4 = 0.6$ m, $\beta_3 = \pi/30$, $\beta_4 = \pi/6$, respectively, on both sides of the shell. With uniform light irradiations to all actuator segments, the control factors for the first four modes are presented in Table 3. Figure 5 shows the modal amplitude of the (1, 1) mode for this configuration. By examining Figs. 4 and 5, it is observed that the (1, 1) modal control effect decreases in configuration 2, as compared with the configuration 1. However, comparison between Tables 2 and 3 shows that this arrangement actually enhances control effects over the asymmetric modes. Hence, the overall controllability of the cylindrical shell can be improved. This increased effectiveness is attributed to the actuators placed at better locations effective to most of the shell modes.

3. Configuration 3

The photostrictive actuators placed at the center of the shell can be used to control the first mode of the shell. By examining the results from configurations 1 and 2, it can be expected that the use of two actuators, each measuring by 24 cm × 10 cm, with the actuators placed at the center can improve control over the modes. As for configurations 2 and 1, the control factors for the first four modes are listed in Table 4. The comparison of the results presented in Tables 2–4 shows that configuration 3 provides the best performance of suppressing the shell oscillations.

B. Comparison of Membrane and Bending Control Effects

To compare the effective control effects introduced by the electric membrane force and bending moment, configuration 2 is considered. The resultant control action can be divided into a membrane control

Table 4 Control factors of configuration 3

Mode	Control factor
(1, 1)	2.453E5
(1, 2)	7.488E4
(2, 1)	4.351E4
(2, 2)	7.474E4

Table 5 Comparison of membrane and bending control effects

Λ_{mn},%	$m=1$	$m=2$	$m=3$
$n=1$	0.3991	3.2620	1.4307
$n=2$	1.1219	2.0522	0.5274
$n=3$	1.8833	10.2444	9.6342

Table 6 Control factors of configuration 4

Mode	Control factor
(1, 1)	1.616E5
(1, 2)	1.549E5
(2, 1)	4.182E4
(2, 2)	4.010E4

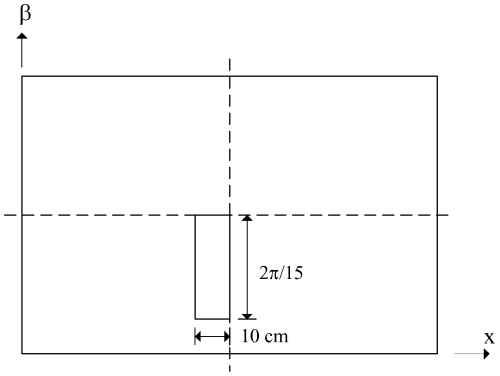

Fig. 6 Configuration 4.

action and a bending control action. Recall that the first two terms of Eq. (29) are related to the bending effect, and the third term is contributed by the membrane effect. The percentage of bending contributions to the total control action are calculated and summarized in Table 5:

$$\Lambda_{mn}(\%) = \frac{\text{bending}}{\text{membrane} + \text{bending}} = \frac{\tilde{M}_{mnx} + \tilde{M}_{mn\beta}}{\tilde{N}_{mn\beta} + \tilde{M}_{mnx} + \tilde{M}_{mn\beta}} \tag{35}$$

A glance at Table 5 reveals that the membrane force control effect is much larger than that of the bending moment for most of the modes. The bending effect is relatively insignificant for the lower modes. These calculations show that the circumferential membrane control effect is the dominating control action for the lower shell modes. In general, the contribution of bending effects increases as the mode number increases. The variations are affected by the individual mode shape function.

C. Reconfiguring the Actuator Layout

Analysis of the membrane and bending contributions to the overall control effect suggests that the actuator patch along the circumferential β direction mainly contributes to the membrane control capability. Therefore, it is expected that by removing the actuator along the longitudinal x direction in configuration II the control factor should not change significantly. The new actuator layout (i.e., configuration 4) is displayed in Fig. 6. Table 6 summarizes the control factors of the first four shell modes of this new layout. Comparison between Tables 3 and 6 does not show substantial differences. This finding demonstrates again that the membrane control effect is the dominating control action for the lower shell modes.

Table 7 Control factors of configuration 5

Mode	Control factor
(1, 1)	2.449E5
(1, 2)	7.481E4
(2, 1)	4.310E4
(2, 2)	7.417E4

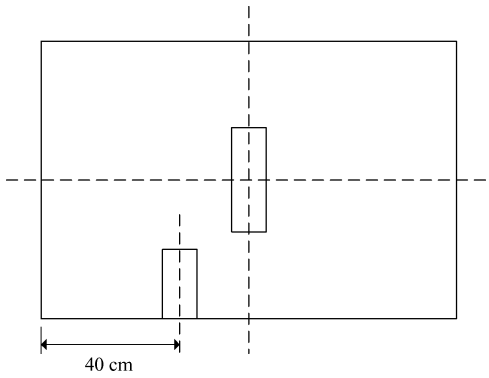

Fig. 7 Configuration 5.

For additional comparison, the configuration 3 is considered. Similarly, removing the actuator patches along the longitudinal direction, the new layout (configuration 5) is shown in Fig. 7. Table 7 shows the control factors for the configuration 5. The results presented in Table 7 show a very small decrease as compared with those presented in Table 4. Therefore, there is a slight reduction in the control effectiveness by removing a half-amount of the optical actuators. This finding implies that it would be effective to lay the photostrictive patches only along the circumferential β axis to control the shell structures when overall control cost is considered.

VII. Conclusions

The photostricitve actuator is a new class of distributed actuator that can induce noncontact distributed actuation without hard-wired connections because of the photodeformation effect. This study focuses on noncontact photonic control of cylindrical shells with segmented optical photostrictive actuators. A mathematical formulation was presented for modeling the coupled mechanical, electrical, optical, and thermal behavior of this optically driven actuator. Definitions of the photodeformation-induced forces and moments of the optical actuator patches were derived. These control forces and bending moments can be used to suppress the structural vibrations. Such optically triggered, noncontact actuators could be desirable for exploration of hazardous and hard to reach locations.

In this paper, the model of a cylindrical shell with surface-bonded discrete photostricitve actuator patches was developed; solution procedures based on the modal expansion method were outlined. The location of the actuator strongly influences the ability of the actuator to control certain modes. The actuator's performance could be degraded by poor placement. To maximize the photoactuation efficiency and optimize the structural performance, the actuator control effectiveness was evaluated with respect to actuator placements. Analytical results obtained here indicate that 1) it appears possible to suppress modes in shell structures using segmented photostrictive actuator patches, 2) the use of an array of strategically placed actuators can provide good controllability of the structure, 3) the bending control effect is relatively insignificant as compared with the membrane control effect, and 4) the actuator along the circumferential β axis is much more effective than the longitudinal x actuator for controlling the simply supported cylindrical shells.

Acknowledgments

The support of the U.S. Army Tank-Automotive and Armaments Command (Contract DAAE07-99-C-L064) and NASA (Grant NAG8-1867) is greatly appreciated.

References

[1]Crawley, E. F., "Intelligent Structures for Aerospace: A Technology Overview and Assessment," *AIAA Journal*, Vol. 32, No. 8, 1994, pp. 1689–1699.

[2]Rogers, C. A., "Intelligent Material Systems—The Dawn of a New Materials Age," *Journal of Intelligent Material Systems and Structures*, Vol. 4, 1993, pp. 4–12.

[3]Tzou, H. S., "Multifield Transducers, Devices, Mechatronic Systems, and Structronic Systems with Smart Materials," *Shock and Vibration Digest*, Vol. 30, No. 4, 1998, pp. 282–294.

[4]Chu, S. Y., Zhou, Y., and Uchino, K., "Photovoltaic Effect for the Linearly Polarized Light in (Pb, La)(Zr, Ti)O_3 Ceramics," *Journal of Smart Material and Structure*, Vol. 3, 1994. pp. 114–117.

[5]Fukuda, T., Hattori, S., Arai, F., Matsuura, H., Hiramatsu, T., Ikeda, Y., and Maekawa, A., "Characteristics of Optical Actuator—Servomechanisms Using Bimorph Optical Piezoelectric Actuator," *Proceedings of 1993 IEEE Robotics and Automation Conference*, Inst. of Electrical and Electronics Engineers, New York, 1993, pp. 618–623.

[6]Uchino, K., "Photostrictive Actuators," *Proceedings of 1990 IEEE Ultrasonics Symposium*, Inst. of Electrical and Electronics Engineers, New York, 1990, pp. 721–723.

[7]Brody, P. S., "Optomechanical Bimorph Actuator," *Ferroelectrics*, Vol. 50, 1983, pp. 27–32.

[8]Liu, B., and Tzou, H. S., "Distributed Photostrictive Actuation and Opto-Piezothermoelasticity Applied to Vibration Control of Plates," *Journal of Vibration and Acoustics*, Vol. 120, 1998, pp. 937–943.

[9]Shih, H. -R., and Tzou, H. S., "Opto-Piezothermoelastic Constitutive Modeling of a New 2-D Photostrictive Composite Plate Actuator," *Proceedings of 2000 ASME International Mechanical Engineering Congress and Exposition*, AD-Vol. 61, edited by H. S. Tzou, M. F. Golnaraghi, and C. J. Radcliffe, American Society of Mechanical Engineers, New York, 2000, pp. 1–8.

[10]Shih, H. -R., and Tzou, H. S., "A New Class of Distributed Photostrictive Orthogonal Actuators in Smart Curved Structures," *Proceedings of 2001 ASME International Mechanical Engineering Congress and Exposition*, IMECE/AD-23721, American Society of Mechanical Engineers, New York, 2001.

[11]Tzou, H. S., *Piezoelectric Shells (Distributed Sensing and Control of Continua)*, Kluwer, Dordrecht, The Netherlands, 1993.

[12]Ventsel, E., and Krauthammer, T., *Thin Plates and Shells, Theory, Analysis, and Applications*, Marcel Dekker, New York, 2001.

R. Lucht
Associate Editor